Wacks DH, Chakraborty N, Klein M, Arias PG, Im HG.

Flow topologies in different regimes of premixed turbulent combustion: A direct numerical simulation analysis.

***Physical Review Fluids* 2016, 1(8), 083401.**

Flow topologies in different regimes of premixed turbulent combustion: a direct numerical simulation analysis

Daniel H. Wacks[1], Nilanjan Chakraborty[1*] , Markus Klein[2], Paul G. Arias[3], Hong G. Im[4]

[1]School of Mechanical and Systems Engineering
University of Newcastle
Claremont Road, Newcastle
NE1 7RU, UK
Email: daniel.wacks@ncl.ac.uk ; nilanjan.chakraboty@ncl.ac.uk

[2]Universität der Bundeswehr München, Fakultät für Luft- und Raumfahrttechnik, LRT1,
Werner-Heisenberg-Weg 39, 85577 Neubiberg, Germany
Email: markus.klein@unibw.de

[3]Department of Mechanical Engineering, University of Michigan,
Ann Arbor, MI 48109-2125, USA
Email: pgarias@umich.edu

[4]Clean Combustion Research Center, King Abdullah University of Science and Technology (KAUST),
Thuwal 23955-6900, Saudi Arabia
Email: hong.im@kaust.edu.sa

[*] Corresponding author

ABSTRACT

The distributions of flow topologies within the flames representing the corrugated flamelets, thin reaction zones and broken reaction zones regimes of premixed turbulent combustion were investigated using direct numerical simulation (DNS) data of statistically planar turbulent H_2-air flames with equivalence ratio $\phi = 0.7$. It was found that the diminishing influence of dilatation rate with increasing Karlovitz number has significant influences on the statistical behaviours of the first, second and third invariants (i.e. P, Q and R) of the velocity gradient tensor. These differences are reflected in the distributions of the flow topologies within the flames considered in this analysis. This has important consequences for those topologies which make dominant contributions to the scalar-turbulence interaction and vortex-stretching terms in the scalar dissipation rate and enstrophy transport equations respectively. Detailed physical explanations were provided for the observed regime dependences of the flow topologies and their implications on the scalar dissipation rate and enstrophy transport.

Keywords: Corrugated flamelets regime; Thin reaction zones regime; Broken reaction zones regime; Flow topology; Direct numerical simulation

I. INTRODUCTION

Turbulent flow fields often exhibit organised flow topologies in spite of their apparent chaotic nature. Perry and Chong [1] and Chong *et al.* [2] assigned all possible local small-scale three-dimensional flow topologies to 8 categories based on the invariants, P, Q and R of the velocity-gradient tensor, $A_{ij} = \partial u_i/\partial x_j$, where u_i is the i^{th} component of velocity vector. The topologies, denoted $\mathrm{S1} - \mathrm{S8}$, distinguish 8 regions in the three-dimensional $P - Q - R$ phase space, as described in Fig. 1. Several previous studies [3-8] analysed the flow properties in the $Q - R$ plane for incompressible fluids (i.e. $P = -\nabla \cdot \vec{u} = 0$). For compressible flows ($P \neq 0$), however, one needs to account for $P - Q - R$ space [9-11]. The analyses of topologies in non-reacting compressible flow turbulence have indicated that the unstable node/saddle/saddle and stable focal/stretching topologies in the $Q - R$ plane dominate over other topologies.

In comparison to the large body of literature on local flow topologies in non-reacting turbulent flows, relatively little attention has been paid to their analysis in turbulent reacting flows [13-16]. Tanahashi *et al.* [13] used Q to distinguish strain-dominated and vorticity-dominated regions in a premixed flame, and concluded that the vorticity vector remains perpendicular to the flame normal vector and that small-scale turbulence can survive even beyond the flame-front. Grout *et al.* [14] analysed the local flow topology of a non-premixed jet in cross-flow, and reported that the highest heat release rates of the flame are associated with the regions with S8 topology. Recently, Cifuentes and coworkers [15,16] analysed the topology distribution in a premixed turbulent flame based on a simple chemistry direct numerical simulations (DNS) database representing the flamelet combustion and demonstrated that the probability of finding focal (i.e. vortical) topologies decreases from the unburned gas side to the burned gas side. However, the differences in flow topology distribution within the flame for different regimes of premixed turbulent combustion are yet to be analysed in the existing literature. These

differences have important consequences on the scalar-turbulence interaction and vortex-stretching terms in the scalar dissipation rate (SDR) and enstrophy transport equations, respectively [17,18]. Thus, the main objectives of this paper are (a) to identify the differences in the distribution of flow topologies in turbulent premixed flames representing different regimes of combustion; and (b) to indicate the implications of the differences in topology distributions on the scalar-turbulence interaction and vortex-stretching terms.

A three-dimensional DNS database of statistically planar turbulent premixed H_2-air flames with equivalence ratio $\phi = 0.7$ [19] has been considered spanning different regimes of premixed combustion. The rest of the paper will be organised as follows. The mathematical background and numerical implementation pertaining to the current analysis will be presented in the next section. This will be followed by presentation of results and their subsequent discussion. Finally, the main findings will be summarised and conclusions will be drawn in the final section of this paper.

II. MATHEMATICAL BACKGROUND & NUMERICAL IMPLEMENTATION

Premixed combustion is often characterised using the non-dimensional temperature, $c_T = (T - T_0)/(T_{ad} - T_0)$ which increases from zero to unity from unburned to burned gases, where T, T_0 and T_{ad} are the dimensional, unburned gas and the adiabatic flame temperature, respectively. The local flow topologies can be characterised by the invariants of the velocity-gradient tensor [1,2]: $A_{ij} = \partial u_i/\partial x_j = S_{ij} + W_{ij}$, where $S_{ij} = 0.5(A_{ij} + A_{ji})$ and $W_{ij} = 0.5\left(A_{ij} - A_{ji}\right)$ are the symmetric and anti-symmetric components, respectively. Three eigenvalues, λ_1, λ_2 and λ_3, of A_{ij} are the solutions of the characteristic equation $\lambda^3 + P\lambda^2 + Q\lambda + R = 0$ where P, Q, R are the invariants of A_{ij} [1,2]:

$$P = -(\lambda_1 + \lambda_2 + \lambda_3);\ Q = 0.5\left(P^2 - S_{ij}S_{ij} + W_{ij}W_{ij}\right);$$
$$R = (-P^3 + 3PQ - S_{ij}S_{jk}S_{ki} - 3W_{ij}W_{jk}S_{ki})/3 \quad (1)$$

The discriminant, $D = [27R^2 + (4P^3 - 18PQ)R + 4Q^3 - P^2Q^2]/108$, of $\lambda^3 + P\lambda^2 + Q\lambda + R = 0$ divides the $P - Q - R$ phase-space into two regions: for $D > 0$ ($D < 0$), A_{ij} displays a focal (nodal) topology [1,2]. The velocity gradient tensor shows one real eigenvalue and two complex conjugate eigenvalues for focal topologies. By contrast, the velocity gradient tensor exhibits three real eigenvalues for nodal topologies. The surface $D = 0$ gives rise to two subsets r_{1a} and r_{1b} in $P - Q - R$ phase space which are given by [1,2]: $r_{1a} = P(Q - 2P^2/9)/3 - 2(-3Q + P^2)^{3/2}/27$ and $r_{1b} = P(Q - 2P^2/9)/3 + 2(-3Q + P^2)^{3/2}/27$. In the region $D > 0$, A_{ij} has purely imaginary eigenvalues on the surface r_2, which are given by $R = PQ$. The surfaces r_{1a}, r_{1b} and r_2 , where r_2 is described by $PQ - R = 0$, divide the $P - Q - R$ phase space into 8 flow topologies, as shown in Fig. 1.

A three-dimensional DNS [19] database of freely-propagating statistically planar turbulent H_2-air premixed flames with $\phi = 0.7$, employing a detailed chemical mechanism [20] with 9 species and 19 chemical reactions, is considered here. An equivalence ratio of 0.7 is chosen because H_2-air mixture for this equivalence ratio is known to be thermo-diffusively neutral [21], such that the additional effects of preferential diffusion are eliminated. The unburned gas temperature T_0 is taken to be 300K, which yields an unstrained laminar burning velocity $S_L = 135.6\ \mathrm{cm/s}$ under atmospheric pressure. The DNS code solves fully compressible Navier-Stokes equations where spatial discretisation is carried out by an 8th order central difference scheme for internal grid points and the order of differentiation gradually decreases to a one-sided 4th order scheme [19]. A fourth order Runge-Kutta scheme is used for explicit time marching [19]. The flame is initialised by a 1D steady initially planar laminar flame profile

[22]. A pre-computed auxiliary divergence free, homogeneous, isotropic turbulence field is generated using a pseudo-spectral method [23] following Passot-Pouquet spectrum [24], and is injected through the inlet. The mean inlet velocity has been changed gradually to match turbulent flame speed as the simulation progresses. In order to assess the extent to which the flames in this study can be qualified as statistically stationary, the temporal evolution of flame area has been monitored and the flame is considered to be statistically stationary when the flame area no longer varies with time. Turbulent inflow and outflow boundaries are taken in the direction of mean flame propagation and transverse boundaries are taken to be periodic. The non-periodic boundaries are specified using an improved Navier Stokes characteristic boundary conditions (NSCBC) technique [25].

The inflow values of normalised root-mean-square turbulent velocity fluctuation u'/S_L , turbulent length scale to flame thickness ratio l_T/δ_{th}, Damköhler number $Da = l_T S_L/u'\delta_{th}$, Karlovitz number $Ka = (\rho_0 S_L \delta_{th}/\mu_0)^{0.5}(u'/S_L)^{1.5}(l_T/\delta_{th})^{-0.5}$ and turbulent Reynolds number $Re_t = \rho_0 u' l_T/\mu_0$ for all cases are presented in Table 1 where μ_0 is the unburned gas viscosity, $\delta_{th} = (T_{ad} - T_0)/\max|\nabla T|_L$ is the thermal flame thickness and the subscript 'L' is used to refer to unstrained laminar flame quantities. The turbulent length scale l_T is the most energetic scale of the Passot-Pouquet spectrum. The cases investigated in this study are nominally representative of three regimes of combustion: case A: corrugated flamelets ($Ka < 1$), case B: thin reaction zones ($1 < Ka < 100$) and case C: broken reaction zones regime ($Ka > 100$) [26]. It is worth noting from Table 1 that Ka in cases A-C is not modified independently of Da and Re_t , and thus the differences in behaviour between cases A-C should not be equated solely to the influences of Karlovitz number Ka. Instead cases A-C, for the purpose of this paper, should be considered as three typical representative scenarios of the

corrugated flamelets, thin reaction zones and broken reaction zones regimes of premixed turbulent combustion, respectively.

The domain size is $20mm \times 10mm \times 10mm$ ($8mm \times 2mm \times 2mm$) in cases A and B (case C) and the domain has been discretised by a uniform Cartesian grid of $512 \times 256 \times 256$ ($1280 \times 320 \times 320$) cells. The smaller domain for case C is justified by the fact that the integral scale l_T is smaller in case C than cases A and B (see Table 1). The grid spacing was determined by the flame resolution, ensuring about 10 grid points across δ_{th}, and in all cases the Kolmogorov length scale remains bigger than the grid spacing (i.e. $\eta \geq 1.5\Delta x$ where η and Δx are the Kolmogorov length scale and DNS grid spacing, respectively). For this resolution about 7-9 grid points reside across the thinnest species gradient. Case C has the highest value of turbulent Reynolds number and thus this case requires the smallest grid spacing to resolve the Kolmogorov length and flame thickness among all the cases considered here. For the purpose of computational economy a smaller computational domain than cases A and B has been chosen here for case C. Simulations have been carried out for $1.0t_e, 6.8t_e$ and $6.7t_e$ (i.e. $t_e = l_T/u'$) for cases A-C respectively, and this simulation time remains comparable to several previous analyses [15,16,27-29].

III. RESULTS & DISCUSSION

Selected regions of instantaneous non-dimensional temperature c_T, normalised first invariant $P^* = P \times (\delta_{th}/S_L)$, second invariant, $Q^* = Q \times (\delta_{th}/S_L)^2$, and third invariant $R^* = R \times (\delta_{th}/S_L)^3$ fields when the statistics were extracted are shown in Fig. 2. Figure 2 also shows the flame location by the contour lines of $c_T = 0.1,0.5,0.7$ overlaid on reaction progress variable field. The c_T-contours clearly show the increasing level of flame wrinkling as the turbulence intensity increases from cases A to C. In cases A and B the c_T-isosurfaces lie close

together, whereas in case C they are both much further apart and the distance between neighbouring isosurfaces varies greatly. This distinction is indicative of the different combustion regimes, which is often characterised in terms of the Karlovitz number. The Karlovitz number can be scaled as $Ka \sim \delta_{th}^2/\eta^2$ where η is the Kolmogorov length scale.

Since δ_{th} remains smaller than η in case A ($\delta_{th} \approx 0.9\eta, \delta_r \approx 0.1\eta$), the flame undergoes no significant velocity fluctuations, which are dissipated at scales of the flame thickness. Eddies with sizes above the Kolmogorov scale wrinkle the flame. Since the reaction zone remains much thinner ($\delta_r \sim 0.1\ \delta_{th}$) it retains its quasi-laminar structure. In case B, on the other hand ($\delta_{th} \approx 3.8\eta, \delta_r \approx 0.4\eta$), eddies with sizes smaller than 4 times the Kolmogorov scale modify the internal structure of the flame thermal thickness, while rest of the larger eddies only wrinkle the flame. Case C represents the broken reaction zones regime ($\delta_{th} \approx 11.2\eta, \delta_r \approx 1.1\eta$), in which eddies with sizes smaller than 11 times the Kolmogorov scale modify the internal structure of the flame thermal thickness, and the eddies at the Kolmogorov scale might modify the internal structure of the reaction thickness. Eddies with sizes greater than 11 times the Kolmogorov scale wrinkle the flame strongly, resulting in a considerable distortion of flame structure. This is evident from significant thickening of the flame and the large variations in the local flame thickness depending on the local turbulent flow conditions.

Note that there are no signs of localised flame extinction in case C in spite of large values of Karlovitz number (i.e. $Ka > 100$). This is consistent with several previous DNS findings [30-33]. The above discussion suggests that distinctly different physical mechanisms are likely to govern the behaviour of invariants in the three cases considered. It is also important to note from Table 1 that the values of Da, Ka and Re_t change from one case to another here and Ka is not modified in isolation. Thus, the alternations of Da and Re_t in addition to the modification

of Ka, play a significant role in the differences in behaviour of the invariants and their components between cases A to C.

Figure 2 shows that the qualitative nature of the distributions of Q^* and R^* in cases B and C is significantly different in comparison to case A: the distributions of Q^* and R^* in case B and C exhibit much smaller length scales than in case A. Note that case B has much higher turbulent Reynolds number Re_t than in case A, and thus case B shows a larger range of length scales than in case A. Cases A and B have same values of l_T but case B shows smaller structures of turbulence in Q^* and R^* distributions due to larger scale separation arising from higher value of Re_t. Case C has a smaller value l_T and a greater value of Re_t than in case A and thus case C exhibits much smaller turbulence structures in Q^* and R^* distributions than in case A due to the combination of higher Re_t and smaller l_T.

It is also seen from Fig. 2 that large non-zero values of P are concentrated within the flame because P is directly related to the dilatation rate (i.e. $P = -\nabla.\vec{u}$), and the effects of thermal expansion and dilatation rate are strong only within the flame. Furthermore, focusing of heat gives rise to high magnitudes of positive $\nabla.\vec{u}$ (i.e. negative values of P with high magnitude) at the locations where the flame is concave towards the reactants. In contrast, defocusing of heat leads to small positive and in some extreme cases negative values of $\nabla.\vec{u}$ (i.e. small negative and positive values of P) at the locations where the flame is convex towards the reactants. [1]

[1] It is not clearly evident from the plane shown in Fig. 2 but this occurs on other planes.

Both strain rate and vorticity along with dilatation rate (i.e. $-P$) contribute towards the value of Q since $Q_S = 0.5\left(P^2 - S_{ij}S_{ij}\right)$ and $Q_W = W_{ij}W_{ij}/2$ according to $Q = Q_S + Q_W$ (see eq. 1). The sign of Q is indicative of vorticity-dominated regions outside the flame (where $P \approx 0$ for low Mach number flows like the one considered here), for which $Q > 0$, and strain-dominated regions, for which $Q < 0$. Figure 2 shows that both vorticity-dominated and strain-dominated regions exist in all cases outside the flame but the degree of intermittency is much greater in cases B and C than in case A. A comparison of the magnitudes of P and Q from Fig. 2 reveals that the magnitude of P^2 remains smaller than the magnitude of Q in most cases in the flow field and these quantities become comparable only within the flame. An increase in u'/S_L leads to an increase in the magnitude of Q: the maximum value of Q in case C is greater than that in case B, which is greater than that in case A.

Distinct modes of the flame-turbulence interaction are evident by comparing cases B and C in Fig. 2 by the evolution of the Q fields across the flame. The magnitude of Q drops significantly across the flame in case B (see the drop of the magnitude of Q across the $c_T = 0.1$ isosurface in case B in Fig. 2). In contrast, in case C the magnitude of the Q field remains significant throughout the flame-front even beyond $c_T = 0.7$. Finally, the high values of Q are found close to the highly concave (to the reactants) regions in case A. This behaviour arises due to focusing of heat in these regions, leading to an increased volumetric dilatation rate ($\nabla \cdot \vec{u}$) and subsequently Q due to high values of P^2 (since $P = -\nabla \cdot \vec{u}$) (see eq. 1).

The expression for R contained in equation 1 may be rewritten as the sum of the terms which play roles in dissipation rate generation ($-\mathrm{S_{ij}S_{jk}S_{ki}}/3$) and enstrophy production ($\mathrm{PQ_w} - \omega_\mathrm{i}\mathrm{S_{ij}}\omega_\mathrm{j}/4$) in the following manner:

$$\mathrm{R} = \frac{1}{3}\left(-\mathrm{P}^3 + 3\mathrm{PQ} - \mathrm{S_{ij}S_{jk}S_{ki}}\right) - \frac{1}{4}\omega_\mathrm{i}\mathrm{S_{ij}}\omega_\mathrm{j}$$

$$= \underbrace{\tfrac{1}{3}\left(-\mathrm{P}^3 + 3\mathrm{PQ_s} - \mathrm{S_{ij}S_{jk}S_{ki}}\right)}_{\mathrm{R_s}} + \mathrm{PQ_w} - \tfrac{1}{4}\omega_\mathrm{i}\mathrm{S_{ij}}\omega_\mathrm{j} \quad (2)$$

Hence, R* may assume high positive or negative values where there is an imbalance of the terms contributing to dissipation rate generation and production of enstrophy. It is evident from Fig. 2 that, in case A, this imbalance is most pronounced in the vicinity of the flame front, whereas in both cases B and C it is evident throughout the entire unburnt gas region. In all three cases the magnitude of R* is negligible in most of the burnt gas region. Furthermore, in case A, the non-negligible values of R* retain the same sign along most of the flame front shown here, whereas, in cases B and C, both positive and negative values of R* co-exist in the unburnt gas region and within the flame front.

Figures 3-6 show the variations of the normalised mean values of P, Q, R and their constituent terms conditional on c_T. The dilatation rate $\nabla \cdot \vec{u} = -P$ remains predominantly positive in turbulent premixed flames but it is possible to get some localised pockets of negative dilatation rate (i.e. $P > 0$) in the regions of the flame which are convex to the reactants (see Fig. 2). However, the probability of finding negative dilatation rate remains smaller than obtaining positive $\nabla \cdot \vec{u}$ and thus the mean values of $P = -\nabla \cdot \vec{u}$ remains negative for all cases considered here (see Fig. 3). The magnitude of $P = -\nabla \cdot \vec{u}$ depends on the strength of chemical activity within the flame. Cases A and B exhibit similar variations of P across the flame but the magnitudes are much less in case C. The flame thicknesses in cases A and B are smaller or comparable to the respective η such that the reaction zone remains quasi-laminar and largely unaffected by turbulent fluctuations. Thus, although the turbulence intensity, u'/S_L, of case B is almost an order of magnitude greater than that in case A, the thermal expansion experienced

in both cases is remarkably similar. In case C, however, the turbulent eddies enter into the inner reaction layer of the flame and disrupt the chemical processes, leading to enhanced heat loss to the preheat zone and a reduction in the reaction rate. For this reason the magnitude of $P = -\nabla \cdot \vec{u}$ observed in case C is much lower than that observed in cases A and B. The diminishing strength of dilatation rate $\nabla \cdot \vec{u} = -P$ with increasing Ka is consistent with the modelling assumption by Peters [26].

Figure 4 shows the variation of mean values of $Q \times (\delta_{th}/S_L)^2$, and its components, $\{Q_S, Q_W\} \times (\delta_{th}/S_L)^2$, conditional on c_T. Both $\nabla \cdot \vec{u} = -P$ and $\sqrt{S_{ij}S_{ij}}$ influence the component $Q_S = (P^2 - S_{ij}S_{ij})/2$, whereas the component $Q_W = W_{ij}W_{ij}/2$ depends on enstrophy Ω (i.e. $W_{ij}W_{ij}/2 = \omega_i\omega_i/4 = \Omega/2$ where ω_i is the i^{th} component of vorticity). Since the turbulence intensity, u'/S_L, in case A is low, the main non-zero contribution arises due to P as a result of thermal expansion. For case A, the mean value of Q_W is negligible and the mean variation of Q is dominated by the mean value of Q_S, which assumes predominantly positive values except towards the burned gas side of the flame where effects of P^2 are negligible due to weak dilatation rate $\nabla \cdot \vec{u} = -P$. For case B, the mean value of Q_W remains non-zero and positive across the flame, whereas the mean value of Q_S remains negative for low and high values of c_T, indicating that $S_{ij}S_{ij}$ dominates over P^2. This behaviour originates from weak contributions of dilatation rate $\nabla \cdot \vec{u} = -P$ on both unburned and burned gas sides of the flame (see Fig. 3), and thus the contribution of $Q_S = (P^2 - S_{ij}S_{ij})/2$ is principally governed by $S_{ij}S_{ij}$ in these regions. However, P^2 assumes high values due to large values of dilatation rate $\nabla \cdot \vec{u} = -P$ close to the reaction zone (see Fig. 3), and thus P^2 dominates over $S_{ij}S_{ij}$ to give rise to positive mean value of Q_S for intermediate values of c_T in case B. Thus, the mean value of $Q \times (\delta_{th}/S_L)^2$ remains small at high and low values of c_T, and attains its maximum values at

$c_T \approx 0.2$ where the mean values of Q_S and Q_W are both positive. In contrast to cases A and B, the magnitude of Q and its components at $c_T \approx 0.0$ is far greater in case C. The mean contribution of $Q_S = (P^2 - S_{ij}S_{ij})/2$ remains negative throughout the flame in case C because in this case the effects of dilatation rate $\nabla \cdot \vec{u} = -P$ are too weak to supersede the influences of $S_{ij}S_{ij}$, and thus in this case the behaviour of Q_S is principally governed by $(-S_{ij}S_{ij})/2$.

The quantity Q_s can be expressed as: $Q_s = Q_{s1} + Q_{s2} = P^2/3 - \mathrm{E}/4\nu$ where $\mathrm{E} = (\tau_{ij}\partial u_i/\partial x_j)/\rho$ is the dissipation rate of instantaneous kinetic energy (i.e. $u_i u_i/2$) and ν is the kinematic viscosity. Hence, $Q_s > 0$ ($Q_s < 0$) corresponds to dilatation (dissipation) dominated regions. Using $Q_{s1} = P^2/3 \sim\{\tau\ S_L/\delta_{th}\}^2$ [17,34] and $|Q_{s2}| = |-\mathrm{E}/4\nu| \sim 1/\tau_\eta^2$ (where τ_η is the Kolmogorov time scale) leads to $Q_{s1}/|Q_{s2}| \sim \tau^2 Ka^{-2}$, where $\tau = (T_{ad} - T_0)/T_0$ is the heat release parameter. This suggests that the relative strength of Q_{s1} with respect to Q_{s2} weakens (strengthens) with increasing Ka (heat release). Thus, in case C (where $Ka \gg 1$), the mean behaviour of Q_s is governed by $Q_{s2} = -\mathrm{E}/4\nu$, whereas in case A (where $Ka < 1$) the mean behaviour of Q_s is governed by positive mean value of $Q_{s1} = P^2/3$ for the major part of the flame brush. In case B (where $Ka > 1$), Q_{s1} dominates over Q_{s2} to result in a mean positive value of Q_s only in the region of the flame where the effects of heat release are strong.

In summary, in case C the mean values of Q_S and Q_W largely balance each other, although the mean value of Q remains negative across the entire flame-front, which is opposite to the behaviour of cases A and B.

The third invariant R may be written as $R = R_S + PQ_W - \omega_i S_{ij}\omega_j/4$ where $R_S = (-P^3 + 3PQ_S - S_{ij}S_{jk}S_{ki})/3$ contains a contribution to the dissipation rate generation (i.e. $S_{ij}S_{jk}S_{ki}$),

while ($PQ_W - \omega_i S_{ij} \omega_j/4$) contributes to the enstrophy production rate [6, 16]. Thus, $R > 0$ indicates that the enstrophy production rate dominates over the dissipation rate generation and *vice versa* [6,16]. The contributions of ($PQ_W - \omega_i S_{ij} \omega_j/4$) and R_S appear to balance across the flame-front in cases A and B (see Fig. 5). In both cases the mean value of R_S attains its maximum value, whereas the mean value of PQ_W attains its minimum value, at $c_T \approx 0.25$. In case C, the mean value of R_S is largely balanced by the mean contribution of $-\omega_i S_{ij} \omega_j/4$, which are both an order of magnitude greater than the mean values of PQ_W and R. The mean value of R attains its maximum value at $c_T \approx 0.0$, but also a local maximum is obtained at $c_T \approx 0.20$, and R remains positive across the flame, indicating that the enstrophy production rate dominates over the dissipation rate generation, unlike cases A and B where the mean $R \approx 0$ across the flame.

Finally, Fig. 6 shows the individual terms contributing to R_S: $-P^3/3$, PQ_S, $-S_{ij}S_{jk}S_{ki}/3$. For cases A and B, all terms are approximately zero at $c_T \approx 0.0$ and $c_T \approx 1.0$. The mean value of $(-P^3/3)$ remains positive and is balanced by the mean contributions of PQ_S and $(-1/3\, S_{ij}S_{jk}S_{ki})$ which are both negative in the region $0.15 < c_T < 0.35$ for cases A and B. In contrast, in case C, the mean contributions of $(-P^3/3), PQ_S$ and $(-S_{ij}S_{jk}S_{ki}/3)$ are positive, but they are dominated by the mean value of $(-S_{ij}S_{jk}S_{ki}/3)$ which is related to the dissipation rate generation. One can express $(\nabla \cdot \vec{u})$E as $(\nabla \cdot \vec{u})\mathrm{E} = 4\nu(PQ_s - P^3/3)$. It can be seen from the mean values of PQ_s and $(-P^3/3)$ in Fig. 6 that the mean value of $(PQ_s - P^3/3) = (\nabla \cdot \vec{u})\mathrm{E}/4\nu$ remains positive throughout the flame. As the mean value of $\nabla \cdot \vec{u}$ remains positive, and the correlation between $\nabla \cdot \vec{u}$ and E is not particularly strong, the positive mean value of $(PQ_s - P^3/3)$ in Fig. 6 indicates a positive mean values of $\mathrm{E} = 2\nu(S_{ij}S_{ij} - P^2/3)$.

Figure 7 shows the joint PDF contours of the normalised second and third invariants, $PDF(Q^*, R^*)$, for cases A-C on $c_T = 0.1, 0.5, 0.7$ where $Q^* = Q \times (\delta_{th}/S_L)^2$ and $R^* = R \times (\delta_{th}/S_L)^3$. The behaviour on isosurfaces of higher c_T values is not shown here, since $Q^* \approx 0.0$ for higher values of c_T (see Fig. 4). The joint PDF exhibits a negative correlation between Q^* and R^* [2,5] for all c_T isosurfaces. As c_T is increased, the most probable value of the distribution moves towards the origin (i.e. $Q^* = 0$ and $R^* = 0$).

It is useful to examine the variation of the individual local topologies, S1-S8, across the flame and to see how their variation changes from one case to another. Figures 8a-c show the variation of the volume fraction, VF, of each topology as a function of c_T following the approach adopted by Cifuentes and his co-workers [15,16]. Figure 8 reveals a noticeable difference in the distribution of the flow topology between cases A-C. For case A, both focal and nodal topologies show clear variation with c_T, with S1,3,4 increasing and S2,7,8 decreasing as moving from the unburnt to the burnt gas region. Such trends diminish from case A to case C such that each topology is more uniformly distributed across c_T in case C. In particular, for case C, the S8 nodal topology disappears entirely. The S8 topology is associated with high positive values of dilatation rate ($\nabla \cdot \vec{u} = -P \gg 0$) and thus its probability decreases for case C due to weakening of dilatation rate.

Figure 8d compares the distributions of volume fraction of total combined focal (i.e. S1,S4,S5,S7) and nodal (i.e. S2,S3,S6,S8) topologies between cases A-C. For case A nodal topologies are dominant in the unburnt gas region and focal topologies in the burnt gas region. This contrasts the previous simple chemistry analyses [15,16] which showed that VF of focal topologies decreases from the unburned gas to the burned gas side. The heat release parameter

$\tau = (T_{ad} - T_0)/T_0$ for cases A-C is greater than that used in Refs. [15,16] (6 as opposed to 4) and thus the flame-induced turbulence is stronger in these cases than in the cases analysed in Refs. [15,16], where VF of vortical (focal) topologies decayed across the flame.[2] The strength of vortical structures within the flame-front increases within the flame due to flame-induced turbulence in case A, which is reflected in the increase in VF of focal (i.e. vortical) topologies within the flame. In case C, the flame does not significantly influence the background turbulent flow field and the focal topologies remain dominant across the entire flame-front.

The statistics of flame curvature plays a key role in order to understand the interrelation between the distributions of the flow and flame topologies. The topology of a c_T isosurface can be described in terms of its mean and Gauss curvatures, κ_m and κ_g, respectively following Doppazo *et al.* [7], where $\kappa_m = (\kappa_1 + \kappa_2)/2 = 1/2\,\nabla \cdot (-\nabla c_T/|\nabla c_T|)$ and $\kappa_g = \kappa_1\kappa_2$, in which κ_1 and κ_2 are the principal curvatures [7,16]. In the $\kappa_m - \kappa_g$ plane, the region $\kappa_g > \kappa_m^2$ indicates complex curvatures and thus is non-physical. Moreover, positive (i.e. $\kappa_m > 0$) curvature is associated with the wrinkles which are convex to the reactants, whereas negative (i.e. $\kappa_m < 0$) curvature represents wrinkles which are concave to the reactants (see Fig. 2). The realisable part of $\kappa_m > 0$ ($\kappa_m < 0$) and $\kappa_g > 0$ represents cup convex (cup concave) flame topology. By contrast, $\kappa_m > 0$ ($\kappa_m < 0$) and $\kappa_g < 0$ represents saddle convex (saddle concave) flame topology. The combination of $\kappa_m > 0$ ($\kappa_m < 0$) and $\kappa_g = 0$ represents tile convex (tile concave) flame topology. Figure 9 shows a scatter plot of the mean versus Gaussian curvature for cases A-C conditional on one representative focal (S7) and one nodal tpology (S3). The plots in Fig. 9 are coloured to highlight the highest concentrations of data

[2] The generation of enstrophy due to baroclinic torque is indeed found to be comparable to the magnitude of viscous dissipation of enstrophy in case A, which leads to considerable enstrophy generation within the flame for this case. By contrast, the viscous dissipation of enstrophy dominates over baroclinic torque contribution in cases B and C where the vortex-stretching and viscous dissipation remain the leading order contributors.

points. It is apparent from Fig. 9 that the distribution of topologies S3 and S7 favour $\kappa_m, \kappa_g > 0$ ($\kappa_m < 0$ and $\kappa_g > 0$) for case A (for case C) whereas case B shows a more symmetric distribution. A similar trend is observed for topologies S1, S2 and S8. Topology S4 is more symmetric and for topologies S5-6 there were insufficient data. These results do not reveal any consistent trend between flow and flame topologies based on these results, and a more detailed analysis is needed in this respect.

Figure 1 shows that the topologies are associated with different types of generic flow structures. Thus, the contributions of these topologies to turbulent processes such as micro-mixing characterised by the scalar dissipation rate (SDR), $N_c = D\nabla c_T \cdot \nabla c_T$ (where D is the thermal diffusivity), and enstrophy $\Omega = \vec{\omega} \cdot \vec{\omega}/2$ transport in turbulent premixed flames are of fundamental importance. The transport equations of N_c and Ω are given by [17,18,34,35]:

$$\rho \frac{DN_c}{Dt} = \frac{\partial}{\partial x_j}\left(\rho D \frac{\partial N_c}{\partial x_j}\right) - 2D\frac{Dc_T}{Dt}\frac{\partial c_T}{\partial x_k}\frac{\partial \rho}{\partial x_k} - 2\rho D \underbrace{\frac{\partial c_T}{\partial x_i}\frac{\partial u_i}{\partial x_j}\frac{\partial c_T}{\partial x_j}}_{\Lambda} \quad \text{(3i)}$$

$$+2D\frac{\partial \dot{\omega}_T}{\partial x_k}\frac{\partial c_T}{\partial x_k} - 2\rho D^2 \frac{\partial^2 c_T}{\partial x_k \partial x_i}\frac{\partial^2 c_T}{\partial x_k \partial x_i} + f(D)$$

$$\frac{D\Omega}{Dt} = \underbrace{\omega_i \omega_k \frac{\partial u_i}{\partial x_k}}_{V} - \epsilon_{ijk}\omega_i \frac{1}{\rho^2}\frac{\partial \rho}{\partial x_j}\frac{\partial \tau_{kl}}{\partial x_l} + \quad \text{(3ii)}$$

$$\frac{\epsilon_{ijk}\omega_i}{\rho}\frac{\partial^2 \tau_{kl}}{\partial x_j \partial x_l} - 2\frac{\partial u_k}{\partial x_k}\Omega + \epsilon_{ijk}\frac{\omega_i}{\rho^2}\frac{\partial \rho}{\partial x_j}\frac{\partial p}{\partial x_k}$$

where $\rho, p, \dot{\omega}_T$ and τ_{ij} are the density, pressure, chemical source term and viscous stress tensor respectively and $f(D)$ accounts for the contribution due to diffusivity gradients. The terms $-2\rho D\Lambda$ and V are referred to as the scalar-turbulence interaction and vortex-stretching terms, respectively [17,18,34,35]. The term Λ in eq. 3i can be written as: $\Lambda = (\partial c_T/\partial x_i)(\partial u_i/\partial x_j)(\partial c_T/\partial x_j) = \left(e_\alpha \cos^2\alpha + e_\beta \cos^2\beta + e_\gamma \cos^2\gamma\right)\nabla c_T \cdot \nabla c_T = a_n \nabla c_T \cdot \nabla c_T$ where $a_n = N_i N_j \partial u_i/\partial x_j$ is the normal strain rate with $N_i = -(\partial c_T/\partial x_i)/|\nabla c_T|$ being

the i[th] component of flame normal vector [17]. This suggests that Λ takes positive (negative) value for positive (negative) values of a_n [17]. The expression $\Lambda = \left(e_\alpha \cos^2\alpha + e_\beta \cos^2\beta + e_\gamma \cos^2\gamma\right)\nabla c_T \cdot \nabla c_T = a_n \nabla c_T \cdot \nabla c_T$ indicates that the behaviours of Λ and a_n are governed by the alignment of ∇c_T with local principal strain rates.

As the flow topologies are associated with particular combinations of strain rate and vorticity distributions, they are likely to influence the statistical behaviours of terms Λ and V. These dependences of $\Lambda = (\partial c_T/\partial x_i)(\partial u_i/\partial x_j)(\partial c_T/\partial x_j) = \left(e_\alpha \cos^2\alpha + e_\beta \cos^2\beta + e_\gamma \cos^2\gamma\right)\nabla c_T \cdot \nabla c_T$ and $V = 2\left(e_\alpha \cos^2\alpha' + e_\beta \cos^2\beta' + e_\gamma \cos^2\gamma'\right)\Omega$ arise due to the alignment of ∇c_T and $\vec{\omega}$ with the most extensive (i.e. most positive), intermediate and the most compressive (i.e. most negative) strain rates (i.e. e_α, e_β and e_γ) where α, β, γ $(\alpha', \beta', \gamma')$ are the angles between ∇c_T ($\vec{\omega}$) and the eigenvectors associated with e_α, e_β and e_γ respectively.

The first row of Fig. 10 shows the contribution of different topologies to the mean values of Λ conditional on c_T.[3] Cases A and B show positive mean contributions of Λ for all topologies except for S5 and S6 in case A and S3, S5 and S6 in case B. The mean value of Λ peaks at $c_T \approx 0.25$. In case A, S2 and S7 remain major contributors of Λ, closely followed by S4 and S8, whereas S8 is the primary contributor in case B, followed, in order, by S7, S2, S4, S1 and S3. The absence of contributions of S1 and S3 in case A is due to the scarcity of the corresponding samples at low values of c_T (see Fig. 8a). Although case C also displays peak

[3] The components of Λ and V conditional on topology have not been shown because they deterministically show similar behaviour. For example, the mean values of $(e_\alpha)\nabla c_T \cdot \nabla c_T$ and $2(e_\alpha \cos^2\alpha')\Omega$ conditional on each topology will exhibit positive values due to positive value of e_α. By the same token, the mean values of $\left(e_\gamma \cos^2\gamma\right)\nabla c_T \cdot \nabla c_T$ and $2\left(e_\gamma \cos^2\gamma'\right)\Omega$ conditional on topology will deterministically exhibit negative values for all cases. The magnitudes of these conditional mean values are expected to be different from one case to another because the strain rate magnitude will depend on u'/S_L and l_T/δ_{th}.

mean values of Λ for low c_T, the behaviour of the topologies is vastly different: mean contributions for S1-S7 are mostly negative, with the exception of S8. The peak magnitude of the negative mean value of Λ is obtained for S2 at $c_T \approx 0.15$. Non-negligible contribution is obtained from S5, although the sample size remains small (see Fig. 8c).

A preferential alignment between ∇c_T and e_α (e_γ), characterised by high probability of $\cos^2\alpha \approx 1.0$ ($\cos^2\gamma \approx 1.0$), leads to a positive (negative) Λ [17,34,36-39]. It has been shown elsewhere [17,34,36-39] that ∇c_T preferentially aligns with e_α when the strain rate induced by flame normal acceleration overcomes turbulence straining. In contrast, ∇c_T aligns with e_γ under the dominance of turbulent straining [17,34,36-39]. As the effects of heat release are stronger in the corrugated flamelets and thin reaction zones regime flames (e.g. cases A and B) than in the broken reaction zones regime flames (e.g. case C), ∇c_T shows strong alignment with e_α (e_γ) in cases A and B (case C) and thus leading to positive (negative) value of Λ . Although case C exhibits predominantly negative Λ, the S8 topology is associated with local high positive $\nabla \cdot \vec{u} = -P$ (see Fig. 1) and thus ∇c_T aligns locally with e_α to result in a positive Λ in this region.

A careful comparison reveals that the mean values of Λ conditional on c_T for S1-S4 topologies exhibit positive values due to predominant alignment of ∇c_T with e_α under the action of strong heat release in cases A and B. By contrast, predominant alignment of ∇c_T with e_γ due to weak influences of heat release in case C yields negative mean values of Λ conditional on c_T for S1-S4 topologies. As the flow topologies S5 and S6 are rare occurrences in premixed flames, a consistent trend is not expected for these topologies. The topologies S7 and S8 are associated with positive $\nabla \cdot \vec{u} = -P$ (see Fig. 1) and thus the effects of heat release are strongly felt in these topologies and as a result ∇c_T aligns locally with e_α to yield positive mean values of Λ

conditional on c_T for these topologies in all three cases. However, effects of heat release are weak towards the unburned gas side of the flame and thus the mean value of Λ conditional on c_T exhibits negative values even for S8 topology in case C.

The second row of Fig. 10 shows the contribution of different topologies to the mean values of $V = 2\left(e_\alpha \cos^2\alpha' + e_\beta \cos^2\beta' + e_\gamma \cos^2\gamma'\right)\Omega$ conditional on c_T , which reveals that the mean value of V conditional on c_T for all topologies remain positive for all three cases. The predominant alignment of $\vec{\omega}$ with the intermediate and most extensive principal strain rates (i.e. e_β and e_α) in these cases, in accordance with previous findings [18,32,35], gives rise to positive mean value of V for all cases considered here but both the mean value and the qualitative behaviour vary greatly between cases. In case A, S7 and S8 remain dominant contributors to V between $0.25 < c_T < 0.75$, but no clear peak in their mean contribution is evident. In case B, however, the contribution of S1 is dominant and its mean value shows a clear peak at $c_T \approx 0.25$. Finally, in case C, all non-zero topologies exhibit peak values at $c_T \approx 0.0$, with S4 and S7 attaining the highest mean values of V. Furthermore, in cases B and C, with the exception of S5 in case C, the contributions of all focal topologies of significant presence (i.e. S1,4,7) attain higher values across the entire flame than for all significant nodal topologies (i.e. S2,3,8).

The effects of flame-induced turbulence are the strongest for topologies which are associated with high positive $\nabla \cdot \vec{u} = -P$ in case A (e.g. S7 and S8). This trend weakens with increasing Ka. Thus, the focal topologies associated with positive Q (see Fig. 1: S1, 4, 7) contribute more to V than the nodal topologies S2,3,8. The topologies S4 and S7 are associated with the vortex-stretching (see Fig. 1), and thus they exhibit high positive mean contribution of V in case C. In the absence of significant flame-induced turbulence, Ω decreases within the flame in case C

and the peak mean value of V is obtained at the unburned gas (i.e. $c_T \approx 0.0$) side of the flame front.

IV. CONCLUSIONS

The flow topology distributions in different regimes of premixed turbulent combustion were investigated using DNS data of statistically planar turbulent H_2-air flames with $\phi = 0.7$. The flow topologies were characterised in terms of the first, second and third invariants (i.e. $P = -\nabla \cdot \vec{u}$, Q and R) of velocity gradient tensor, $\partial u_i/\partial x_j$, where invariants Q and R are closely linked with vorticity and strain rates, and also their generation rates. The mean value of $\nabla \cdot \vec{u} = -P$ decreases considerably in the broken reaction zones regime due to the severe disruption in chemical processes. The regime of combustion, especially the weakening of dilatation rate effects with increasing Karlovitz number, significantly affects the statistical behaviours of dilatation rate, enstrophy and strain rate magnitude in addition to the generation rates of enstrophy and dissipation rate. These influences are reflected in the statistical behaviours of the second and third invariants (i.e. Q and R) of the velocity gradient tensor and their behaviour across the flame.

Detailed explanations were provided for the observed combustion regime dependences of P, Q and R, flow topology distribution and their influences on the scalar-turbulence interaction and vortex-stretching terms in the SDR and enstrophy transport equations respectively. It was demonstrated that the influences of combustion regime on P, Q and R have important consequences on the distribution of those flow topologies which make dominant contributions to the scalar-turbulence interaction and vortex-stretching terms in the SDR and enstrophy transport equations respectively. This analysis identifies the flow topologies that make dominant contributions to Λ and V and thus the flow configurations responsible for the observed

trends in different combustion regimes. This information can help in designing simplified experimental configurations for analysing the statistical behaviours of the scalar-turbulence interaction and vortex-stretching terms.

ACKNOWLEDGEMENTS

NC and DHW are grateful to EPSRC and N8/ARCHER. PGA and HGI were sponsored by KAUST and made use of the resources of the KAUST Supercomputing Laboratory and computer clusters.

REFERENCES

1. A. Perry, M. Chong, Ann. Rev. Fluid Mech.,**19**, 125 (1987).

2. M. Chong, A. Perry, B. Cantwell, Phys. Fluids, **2**, 765 (1990).

3. J. Soria, R. Sondergaard, B. Cantwell, M. Chong, A. Perry, Phys. Fluids, **6**, 871 (1994).

4. M. Chong, A. Perry, J. Chacin, B. Cantwell, J. Fluid Mech. **357**, 225 (1998).

5. A. Ooi, J. Martın, J. Soria, M. Chong, J. Fluid Mech., **381**, 141 (1999).

6. J. Chacin, B. Cantwell, J. Fluid Mech., **404**, 87 (2000).

7. C. Dopazo, J. Martin, J. Hierro, J. Phys. Rev. E., **76**, 056316 (2007).

8. E. Elsinga, I. Marusic, J. Fluid Mech., **662**, 514 (2010).

9. J. Chen, B. Cantwell, N. Mansour, Proc. 10th Australasian Fluid Mechanics Conference, Melbourne, Australia, 5.1-5.4 (1989).

10. R. Sondergaard, J. Chen, J. Soria, B. Cantwell, Eighth symposium on turbulent shear flows, Technical University of Munich, 16/1.1–16/1.6 (1991).

11. H. Maekawa, T. Hiyama, Y. Matsuo, JSME Intl J., **42**, 846 (1999).

12. S. Suman and S. Girimaji, J. Turbul., **11**,1 (2010).

13. M. Tanahashi, M. Fujimura, T. Miyauchi, Proc. Comb. Inst., **28**, 529 (2000).

14. R. Grout, A. Gruber, C. Yoo, J. Chen, Proc. Comb. Inst., **33**, 1629 (2011).

15. L. Cifuentes, C. Dopazo, J. Martin, C. Jimenez, Phys. Fluids, **26**, 065108 (2014).

16. L. Cifuentes, Local flow topologies and scalar structures in turbulent combustion, PhD thesis (2015).

17. N. Chakraborty, N. Swaminathan, Phys. Fluids, **19**, 045103 (2007).

18. N. Chakraborty, Eur. J. Mech. Fluids/B, **46**, 201 (2014).

19. H.G. Im, P.G. Arias, S. Chaudhuri, H.A. Uranakara, Direct numerical simulations of statistically stationary turbulent premixed flames, Combust. Sci. Technol., in press (2016).

20. M. P. Burke, M. Chaos, Y. Ju, F.L. Dryer, S.J. Klippenstein, I. J. Chem. Kinetics, **44**, 444 (2012).

21. N. Chakraborty, E.R. Hawkes, J. H. Chen, R.S. Cant, Combust. Flame, **154**, 259-280 (2008).

22. R.J. Kee, J.F. Grcar, M.D. Smooke, J.A. Miller, A FORTRAN Program for Modeling Steady One-Dimensional Premixed Flames, Tech. Rep. SAND85-8240, Sandia National Laboratories (1985).

23. R.S. Rogallo, Numerical experiments in homogeneous turbulence, *NASA Technical Memorandum* 81315, NASA Ames Research Center, California (1981).

24. T. Passot, A. Pouquet, J. Fluid Mech. **181**, 441, (1987).

25. C.S. Yoo, Y. Wang, A. Trouve, H.G. Im, Combust. Theor. Modell., **9**, 617 (2005).

26. N. Peters, Turbulent Combustion, Cambridge University Press (2000).

27. I. Han, K.Y. Huh, Combust. Flame, **152**,194-205(2008).

28. H. Reddy, J. Abraham, Phys. Fluids, **24**,105108 (2012).

29. C. Pera, S. Chevillard, R. Reveillon, Combust. Flame, **160**, 1020 (2013).

30. Z.M. Nikolaou, N. Swaminathan, Combust. Flame, **161,** 3073 (2014) -3084.

31. A.J. Aspden, M.S. Day, J.B. Bell, J. Fluid Mech., **680**, 287 (2011) -320.

32. P.E. Hamlington, A.Y. Poludnenko, E.S. Oran, Phys. Fluids, **23**, 125111 (2011).

33. H. Carlsson, R. Yu, X.S. Bai, Int. J. Hydrogen Energy, **39**, 20216 (2014).

34. N. Chakraborty, M. Champion, A. Mura, N. Swaminathan, N. 2011. Scalar dissipation rate approach to reaction rate closure. In: *Turbulent premixed flame*, N. Swaminathan and K.N.C. Bray, (eds.). Cambridge University Press, 1st Edition, Cambridge, UK, pp. 76-102.

35. A. Tsinober, L. Shtilman, H. Vaisburd, Fluid Dyn. Res. **21**, 477 (1997).

36. N. Chakraborty, N. Swaminathan, Phys. Fluids, **19**, 045103 (2007).

37. S.H. Kim, H. Pitsch, Phys. Fluids, **19**, 115107(2007).

38. N. Chakraborty, M. Klein, N. Swaminathan, Proc. Combust. Inst., **32**,1409 (2009).

39. S.P. Malkeson, N. Chakraborty, Phys. Rev. E. **83**, 046308 (2011).

TABLES

Case	u'/S_L	l_T/δ_{th}	Re_t	Da	Ka
A	0.7	14.0	227	20.0	0.75
B	5	14.0	1623	2.8	14.4
C	14	4.0	1298	0.29	126

Table 1: List of inflow turbulence parameters

FIGURE CAPTIONS

Figure 1: (Top) Classification of $S1-S8$ topologies in the $Q-R$ plane for (left to right) $P>0$, $P=0$ and $P<0$. The lines r_{1a} (red), r_{1b} (blue) and r_2 (green) dividing the topologies are shown. Black dashed lines correspond to $Q=R=0$. (Bottom) Classification of $S1-S8$ topologies: UF=unstable focus, UN=unstable node, SF=stable focus, SN=stable node, S=saddle, C=compressing, ST=stretching.

Figure 2: Selected regions of instantaneous (row 1) reaction progress variable c_{T} (green contours show $c_{\mathrm{T}}=0.1,0.5,0.7$ isolines from left to right, shown in close-up in row 2), (row 3) normalised first invariant $P^*=P\times(\delta_{th}/S_L)$, (row 4) second invariant, $Q^*=Q\times(\delta_{th}/S_L)^2$, and (row 5) third invariant $R^*=R\times(\delta_{th}/S_L)^3$ fields at the $x-y$ mid-plane for (left to right) cases A-C.

Figure 3: Log-linear variation of $\mathrm{P}\times\delta_{th}/S_L$ with c_T for cases A-C (red-green-blue).

Figure 4: Log-linear variation of $Q\times(\delta_{th}/S_L)^2$ (red), $Q_S\times(\delta_{th}/S_L)^2$ (green), $Q_W\times(\delta_{th}/S_L)^2$ (blue) with c_T for cases A-C.

Figure 5: Log-linear variation of $\mathrm{R}\times(\delta_{th}/S_L)^3$ (red), $\mathrm{R_S}\times(\delta_{th}/S_L)^3$ (green), $\mathrm{PQ_W}\times(\delta_{th}/S_L)^3$ (blue) and $(-\omega_{\mathrm{i}}\mathrm{S_{ij}}\omega_{\mathrm{j}}/4)\times(\delta_{th}/S_L)^3$ (magenta) with $\mathrm{c_T}$ for cases A-C. All terms in case C are to be multiplied by 10^4 as indicated.

Figure 6: Log-linear variation of $\{-\mathrm{P}^3/3\}\times(\delta_{th}/S_L)^3$ (red), $\{\mathrm{PQ_S}\}\times(\delta_{th}/S_L)^3$ (green) and $\{-\mathrm{S_{ij}S_{jk}S_{ki}}/3\}\times(\delta_{th}/S_L)^3$ (blue) with c_T for cases A-C. Inset in case C shows variation of terms of smaller magnitude. All terms in case C are to be multiplied by 10^4 as indicated.

Figure 7: Joint PDFs of $Q^*=Q\times(\delta_{th}/S_L)^2$ and $R^*=R\times(\delta_{th}/S_L)^3$, $\mathrm{PDF}(Q^*,R^*)$, on $c_T=0.1,0.5,0.7$ isosusfaces for cases A-C. Value of $\mathrm{PDF}(Q^*,R^*)$ rises from blue to red colour.

Figure 8: Variation of volume fractions VF of topologies S1-8 with reaction progress variable c_T for (a-c) cases A-C: focal topologies S1,4,5,7 (red-blue-green-magenta solid lines) and nodal topologies S2,3,6,8 (red-blue-green-magenta dashed lines). (d) Variation of VF of total focal

(solid lines) and nodal (dashed lines) topologies with c_T for cases A (tan), B (black) and C (olive).

Figure 9: Scatter of normalised mean and Gaussian curvatures coloured by count for (left to right) case A-C. Topologies S3 and S7 are shown exemplarily. Magnitude increases with colour from white to red. Green dots indicate the location of the maximum values.

Figure 10: Variation of the mean values of (first row) $\Lambda^* = \Lambda \times \delta_{\mathrm{th}}^3/\mathrm{S_L}$ and (second row) $\mathrm{V}^* = \mathrm{V} \times (\delta_{\mathrm{th}}/\mathrm{S_L})^3$ conditional on c_T for (1^{st} -3^{rd} columns) cases A-C: focal topologies S1,4,5,7 (red-blue-green-magenta solid lines) and nodal topologies S2,3,6,8 (red-blue-green-magenta dashed lines). Results are omitted where $\mathrm{VF} < 0.01$. The values of V^* in case C are to be multiplied by 10^5 as indicated.

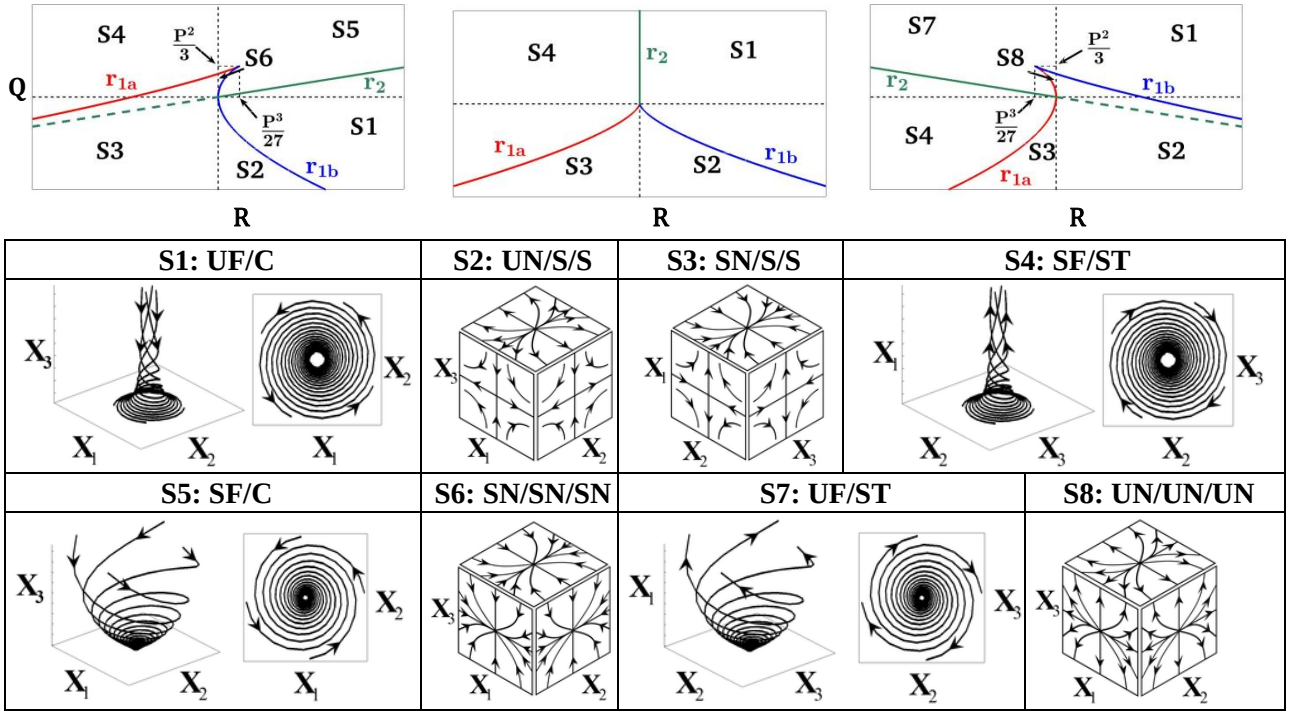

Figure 1: (Top) Classification of $S1-S8$ topologies in the $Q-R$ plane for (left to right) $P>0$, $P=0$ and $P<0$. The lines r_{1a} (red), r_{1b} (blue) and r_2 (green) dividing the topologies are shown. Black dashed lines correspond to $Q=R=0$. (Bottom) Classification of $S1-S8$ topologies: UF=unstable focus, UN=unstable node, SF=stable focus, SN=stable node, S=saddle, C=compressing, ST=stretching.

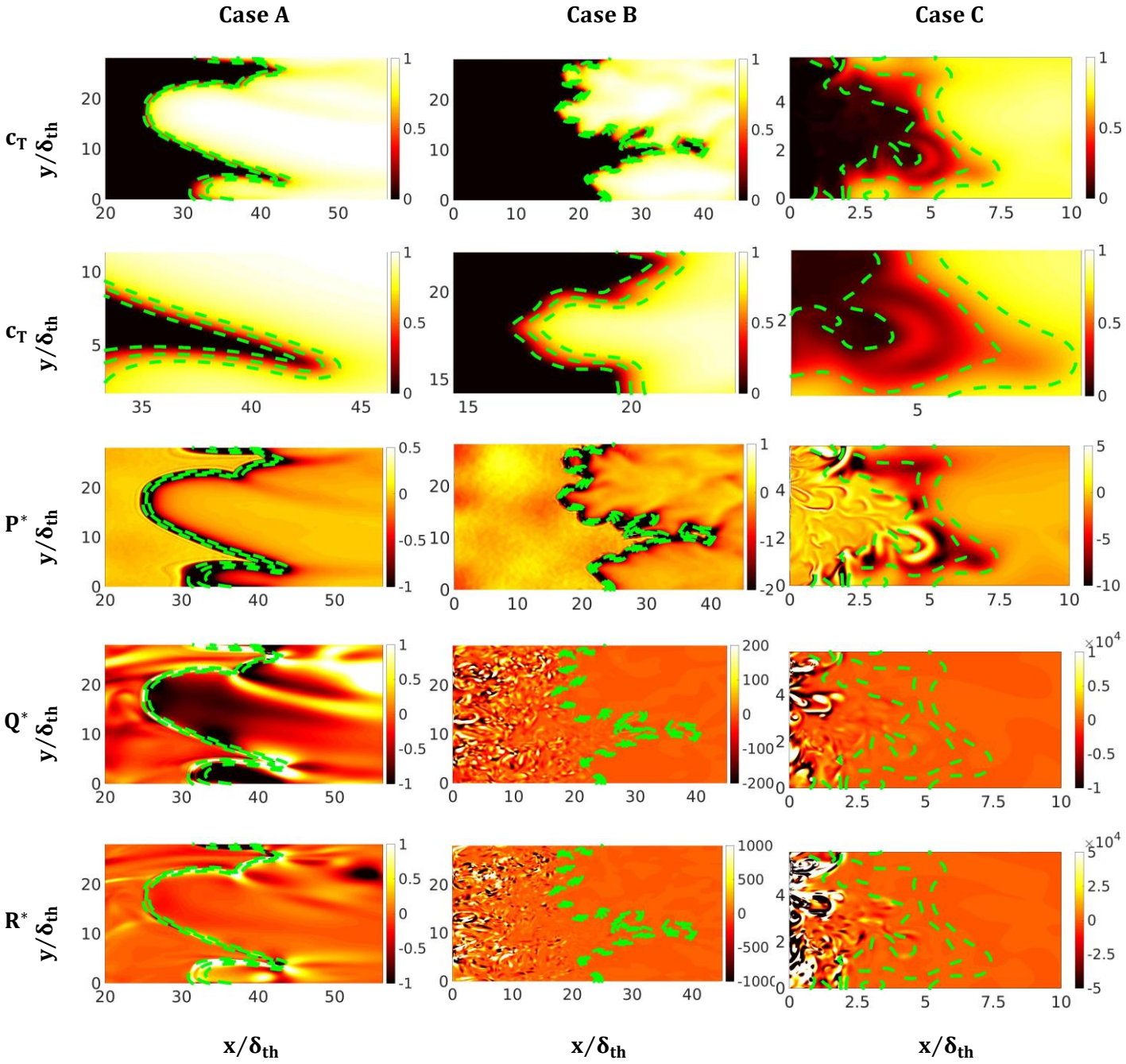

Figure 2: Selected regions of instantaneous (row 1) reaction progress variable c_T (green contours show $c_T = 0.1, 0.5, 0.7$ isolines from left to right, shown in close-up in row 2), (row 3) normalised first invariant $P^* = P \times (\delta_{th}/S_L)$, (row 4) second invariant, $Q^* = Q \times (\delta_{th}/S_L)^2$, and (row 5) third invariant $R^* = R \times (\delta_{th}/S_L)^3$ fields at the $x-y$ mid-plane for (left to right) cases A-C.

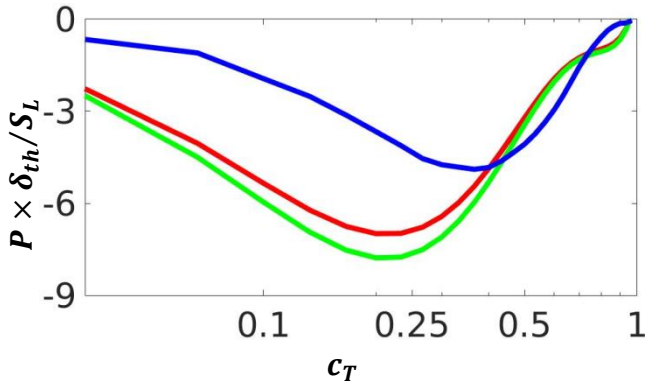

Figure 3: Log-linear variation of $P \times \delta_{th}/S_L$ with c_T for cases A-C (red-green-blue).

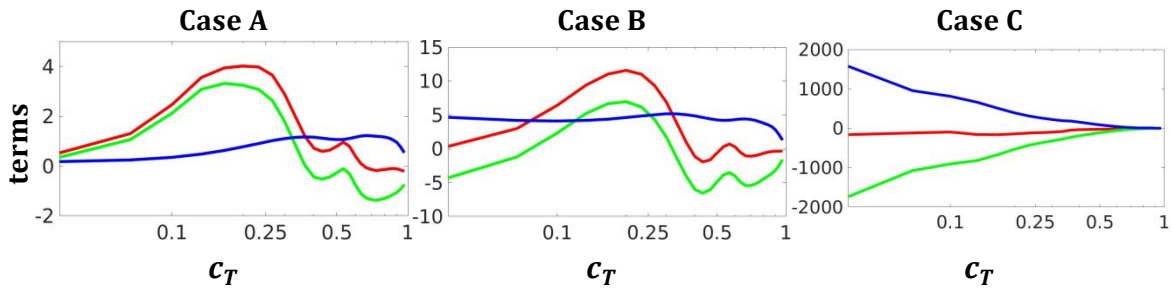

Figure 4: Log-linear variation of $Q \times (\delta_{th}/S_L)^2$ (red), $Q_S \times (\delta_{th}/S_L)^2$ (green), $Q_W \times (\delta_{th}/S_L)^2$ (blue) with c_T for cases A-C.

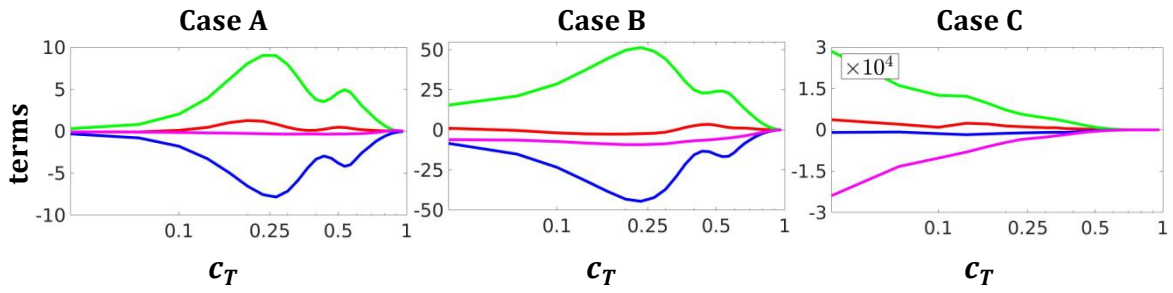

Figure 5: Log-linear variation of $R \times (\delta_{th}/S_L)^3$ (red), $R_S \times (\delta_{th}/S_L)^3$ (green), $PQ_W \times (\delta_{th}/S_L)^3$ (blue) and $(-\omega_i S_{ij} \omega_j/4) \times (\delta_{th}/S_L)^3$ (magenta) with c_T for cases A-C. All terms in case C are to be multiplied by 10^4 as indicated.

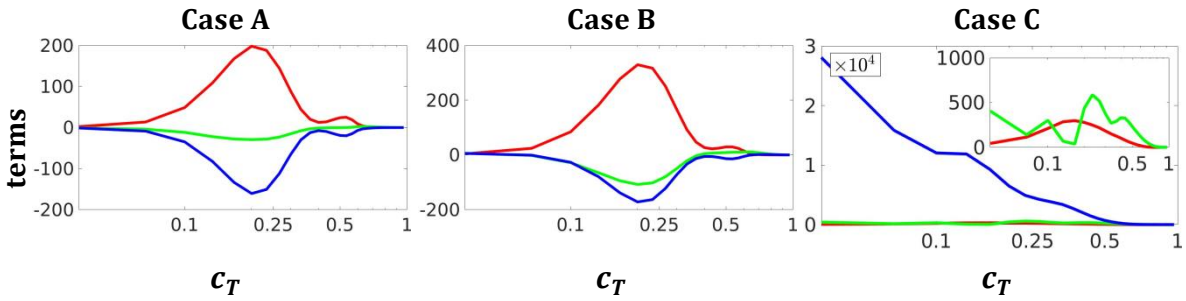

Figure 6: Log-linear variation of $\{-P^3/3\} \times (\delta_{th}/S_L)^3$ (red), $\{PQ_S\} \times (\delta_{th}/S_L)^3$ (green) and $\{-S_{ij}S_{jk}S_{ki}/3\} \times (\delta_{th}/S_L)^3$ (blue) with c_T for cases A-C. Inset in case C shows variation of terms of smaller magnitude. All terms in case C are to be multiplied by 10^4 as indicated.

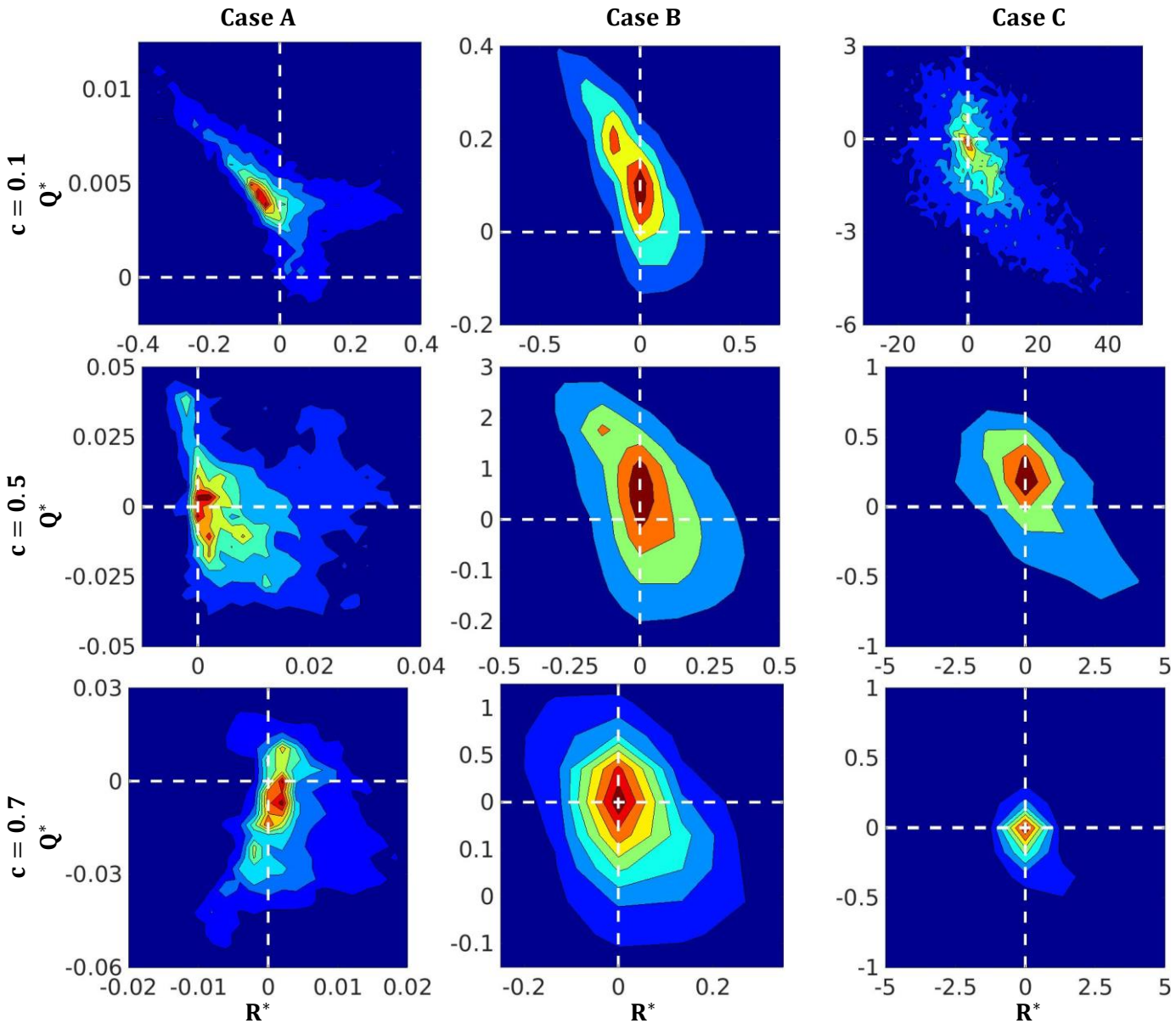

Figure 7: Joint PDFs of $Q^* = Q \times (\delta_{th}/S_L)^2$ and $R^* = R \times (\delta_{th}/S_L)^3$, PDF$(Q^*, R^*)$, on $c_T = 0.1, 0.5, 0.7$ isosusfaces for cases A-C. Value of PDF(Q^*, R^*) rises from blue to red colour.

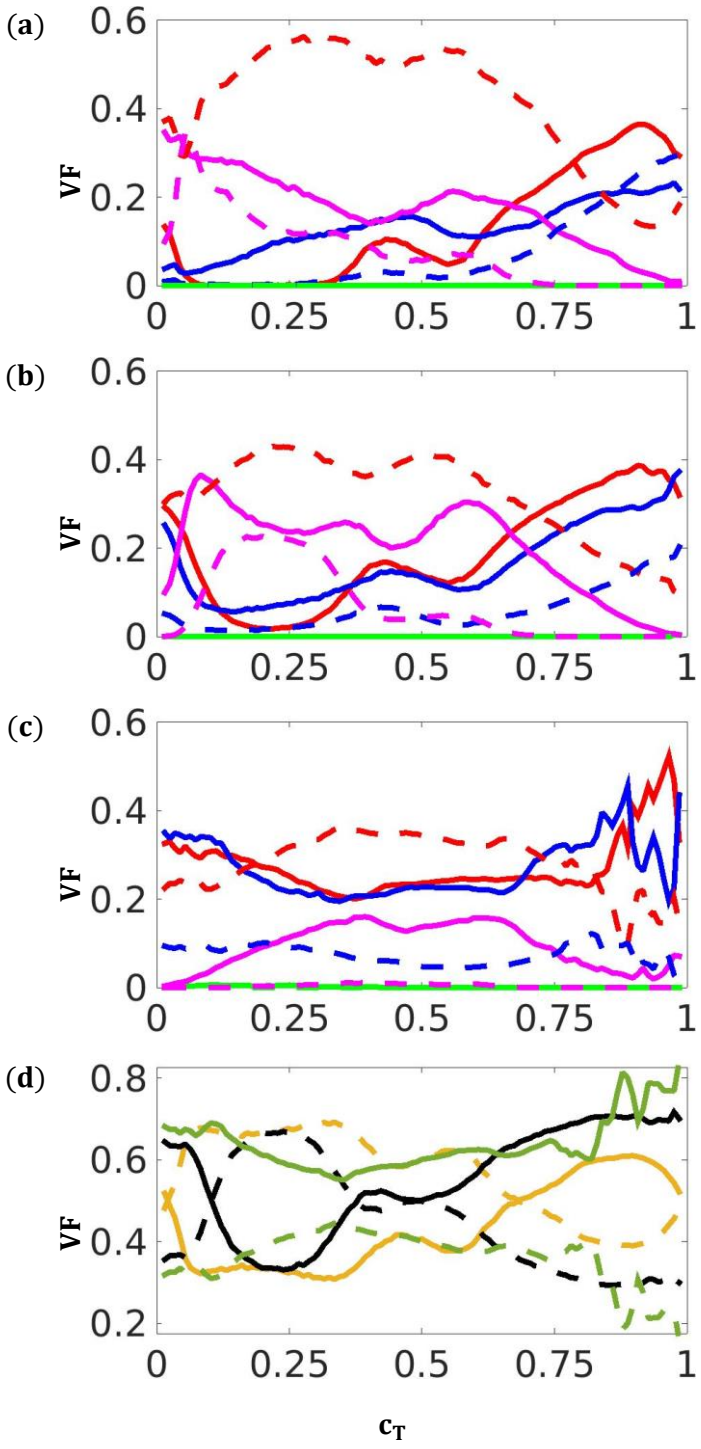

Figure 8: Variation of volume fractions VF of topologies S1-8 with reaction progress variable c_T for (a-c) cases A-C: focal topologies S1,4,5,7 (red-blue-green-magenta solid lines) and nodal topologies S2,3,6,8 (red-blue-green-magenta dashed lines). (d) Variation of VF of total focal (solid lines) and nodal (dashed lines) topologies with c_T for cases A (tan), B (black) and C (olive).

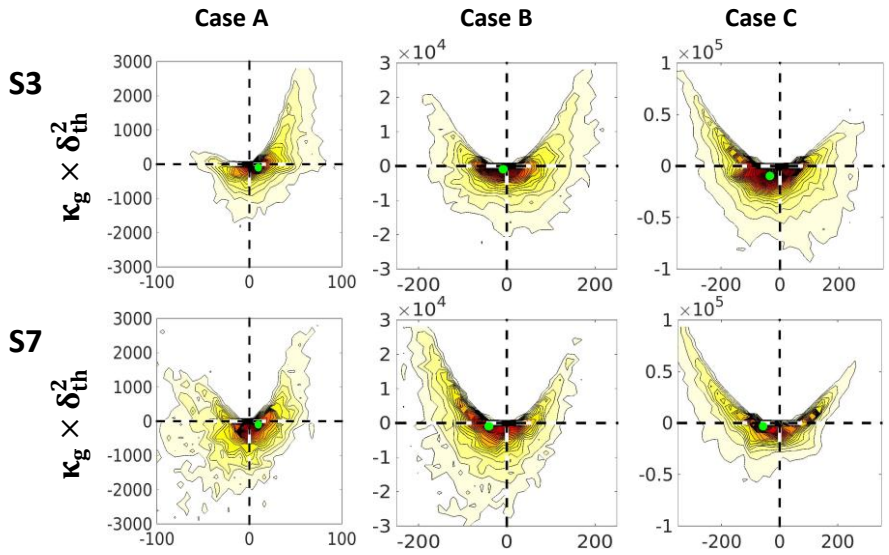

Figure 9: Scatter of normalised mean and Gaussian curvatures coloured by count for (left to right) case A-C. Topologies S3 and S7 are shown exemplarily. Magnitude increases with colour from white to red. Green dots indicate the location of the maximum values.

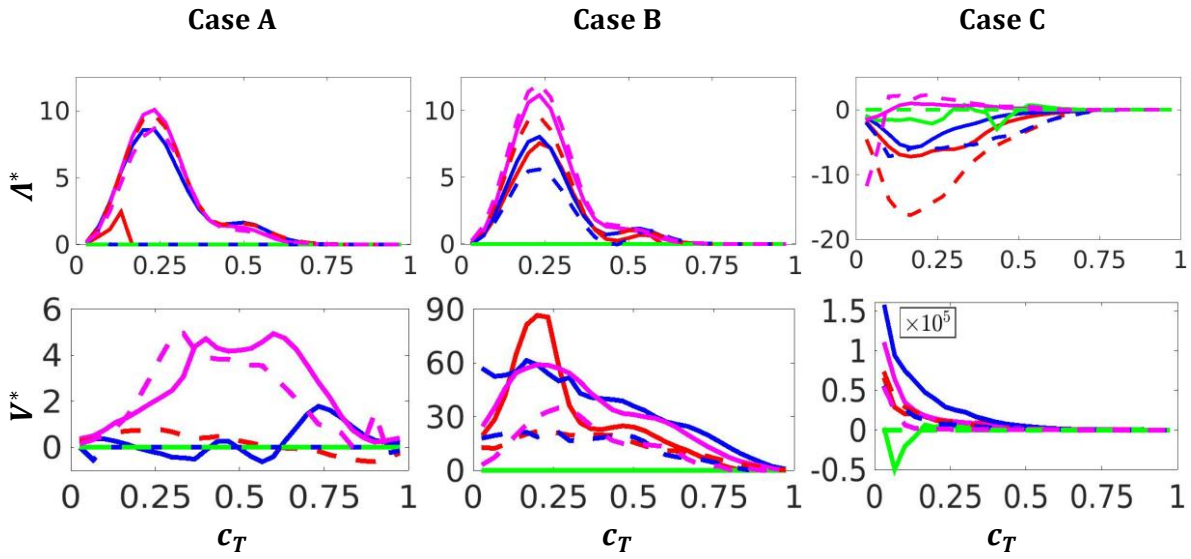

Figure 10: Variation of the mean values of (first row) $\Lambda^* = \Lambda \times \delta_{th}^3/S_L$ and (second row) $V^* = V \times (\delta_{th}/S_L)^3$ conditional on c_T for (1st -3rd columns) cases A-C: focal topologies S1,4,5,7 (red-blue-green-magenta solid lines) and nodal topologies S2,3,6,8 (red-blue-green-magenta dashed lines). Results are omitted where $VF < 0.01$. The values of V^* in case C are to be multiplied by 10^5 as indicated.